

# Exploring dynamical phase transitions with cold atoms in an optical cavity

<https://doi.org/10.1038/s41586-020-2224-x>

Received: 27 September 2019

Accepted: 10 February 2020

Published online: 29 April 2020

 Check for updates

Juan A. Muniz<sup>1,3</sup>, Diego Barberena<sup>1,2,3</sup>, Robert J. Lewis-Swan<sup>1,2,3</sup>, Dylan J. Young<sup>1</sup>, Julia R. K. Cline<sup>1</sup>, Ana Maria Rey<sup>1,2</sup> & James K. Thompson<sup>1</sup>

Interactions between atoms and light in optical cavities provide a means of investigating collective (many-body) quantum physics in controlled environments. Such ensembles of atoms in cavities have been proposed for studying collective quantum spin models, where the atomic internal levels mimic a spin degree of freedom and interact through long-range interactions tunable by changing the cavity parameters<sup>1–4</sup>. Non-classical steady-state phases arising from the interplay between atom–light interactions and dissipation of light from the cavity have previously been investigated<sup>5–11</sup>. These systems also offer the opportunity to study dynamical phases of matter that are precluded from existence at equilibrium but can be stabilized by driving a system out of equilibrium<sup>12–16</sup>, as demonstrated by recent experiments<sup>17–22</sup>. These phases can also display universal behaviours akin to standard equilibrium phase transitions<sup>8,23,24</sup>. Here, we use an ensemble of about a million strontium-88 atoms in an optical cavity to simulate a collective Lipkin–Meshkov–Glick model<sup>25,26</sup>, an iconic model in quantum magnetism, and report the observation of distinct dynamical phases of matter in this system. Our system allows us to probe the dependence of dynamical phase transitions on system size, initial state and other parameters. These observations can be linked to similar dynamical phases in related systems, including the Josephson effect in superfluid helium<sup>27</sup>, or coupled atomic<sup>28</sup> and solid-state polariton<sup>29</sup> condensates. The system itself offers potential for generation of metrologically useful entangled states in optical transitions, which could permit quantum enhancement in state-of-the-art atomic clocks<sup>30,31</sup>.

Arrays of ultracold alkaline-earth atoms with narrow-linewidth optical transitions are the basis of the most precise atomic clocks<sup>31</sup> and are also used for quantum simulation<sup>32</sup> and quantum information processing<sup>33</sup>. When these atoms are placed inside an optical cavity, their long-lived internal levels make them ideal to simulate non-equilibrium quantum magnetism, including models featuring long-range interactions mediated by cavity photons.

Here we report an advance towards the goal of simulating quantum magnetism in an optical cavity. We observe a dynamical phase transition generated by coupling a narrow-linewidth optical transition of an ensemble of strontium atoms to a single detuned cavity mode (Fig. 1a, left).

In general terms, non-equilibrium phase transitions, characterized by the existence of a critical point that separates phases with distinct properties, have been described in various contexts. In driven open systems, non-equilibrium phases are signalled by different steady states that depend on system parameters such as pump or loss rates<sup>9–11,34–36</sup>, independent of initial conditions. Conversely, here we focus on a non-equilibrium phase transition in a closed system—often referred to as a dynamical phase transition (DPT)—where the

non-equilibrium quantum phases are dynamical in nature: that is, qualitatively distinct behaviours are observed below, above or at a critical point<sup>14,37–40</sup> in terms of the time average of an order parameter such as magnetization. DPTs are typically initiated by quenching control parameters and depend on the initial state of the system. Such DPTs have been observed experimentally in arrays of trapped ions<sup>17</sup> and cold gases<sup>20</sup>, as well as previously in the context of macroscopic self-trapping<sup>28,29,41,42</sup>. Here we demonstrate a DPT in a system of cold atoms with global interactions mediated by an optical cavity.

## Implementation of the Lipkin–Meshkov–Glick model

A feature of our cavity simulator (Fig. 1a), compared with earlier observations, is the use of a much larger ensemble of  $N \approx 10^5$ – $10^6$  cold <sup>88</sup>Sr atoms. We use two long-lived electronic levels in these atoms,  $|\downarrow\rangle\langle^1S_0(m_J=0)|$  and  $|\uparrow\rangle\langle^3P_1(m_J=0)|$  states, to mimic a spin-1/2 system ( $|\downarrow\rangle$  and  $|\uparrow\rangle$ , respectively). The atoms are confined in a one-dimensional (1D) optical lattice with a near-magic-wavelength of 813 nm supported by the optical cavity. We operate the experiment

<sup>1</sup>JILA, NIST and Department of Physics, University of Colorado, Boulder, CO, USA. <sup>2</sup>Center for Theory of Quantum Matter, University of Colorado, Boulder, CO, USA. <sup>3</sup>These authors contributed equally: Juan A. Muniz, Diego Barberena, Robert J. Lewis-Swan. <sup>✉</sup>e-mail: arey@jila.colorado.edu; jkt@jila.colorado.edu

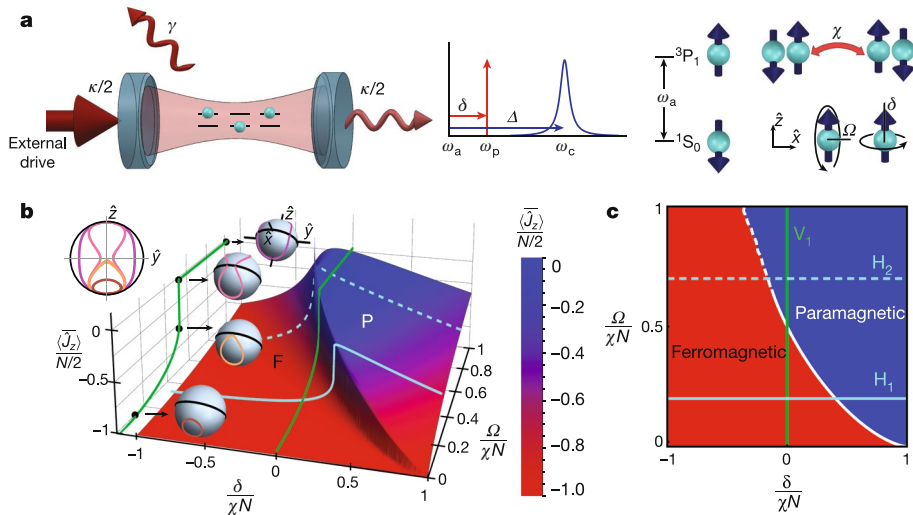


**Fig. 1 | System and dynamical phase diagram.** **a**, An ensemble of  $^{88}\text{Sr}$  atoms is trapped in a 1D optical lattice supported by an optical cavity (left). The atoms are coupled to a single cavity mode with a single-photon Rabi frequency  $2g$  and a resonance frequency  $\omega_c$ , detuned by  $\Delta = \omega_c - \omega_a$  from the optical atomic transition  $|1S_0, m_j = 0 (\downarrow)\rangle$  to  $|3P_1, m_j = 0 (\uparrow)\rangle$  (with frequency  $\omega_a$  and linewidth  $\gamma$ ). Light leaks out of the cavity at a total rate  $\kappa$ . The cavity is driven externally by a laser with frequency  $\omega_p$  that, if on resonance with an empty cavity, would establish a coherent state inside the cavity with average intracavity photon number  $|2\Omega_p/\kappa|^2$ . As shown centre and right, for the far-detuned cavity system in consideration, the external drive generates a transverse field that drives Rabi flopping at frequency  $\Omega = -2g\Omega_p/\Delta$ . The external drive detuning  $\delta = \omega_p - \omega_a$  establishes a longitudinal field. The detuned cavity field generates an effective spin exchange interaction of strength  $\chi = -g^2/\Delta$  (red arrow, right). **b**, The collective LMG model with transverse and longitudinal fields features a second-order DPT between paramagnetic (P, blue) and ferromagnetic

phases (F, red). The DPT is characterized by the long-time average of the collective magnetization  $\langle \hat{j}_z \rangle$ , and its dynamics can be characterized by trajectories of the classical Bloch vector in the pseudospin Bloch sphere (see projection and associated sphere insets). For  $\delta = 0$ , in the paramagnetic phase the trajectories circumnavigate the Bloch sphere, whereas in the ferromagnetic phase the trajectories are trapped below the equator. **c**, The two-dimensional map shows the DPT indicated by a sharp change in  $\langle \hat{j}_z \rangle$  (white solid line) for  $\delta/(\chi N) \geq -1/8$ . The white dashed line ( $\delta/(\chi N) < -1/8$ ) signals a smooth crossover between the two phases (see Methods). Curves for  $\delta = 0$  (green solid line,  $V_1$ ),  $\Omega/(\chi N) = 0.2$  (blue solid line,  $H_1$ ) and  $\Omega/(\chi N) = 0.7$  (blue dashed line,  $H_2$ ) are shown on both diagrams and experimentally investigated in Figs. 2b, 3a and 3b, respectively. The dependence of the transition point on both  $\delta/(\chi N)$  and  $\Omega/(\chi N)$  is investigated in Extended Data Fig. 2b.

in a regime in which the atoms couple to a single common transverse electromagnetic ( $\text{TEM}_{00}$ ) mode of the optical cavity with resonance frequency  $\omega_c$  detuned by  $\Delta = \omega_c - \omega_a$  from the atomic optical transition with frequency  $\omega_a$ . Here  $|\Delta|$  is large with respect to the linewidths of the cavity,  $\kappa/(2\pi) = 153.0(4)$  kHz, and atomic transition,  $\gamma/(2\pi) = 7.5$  kHz, and also the vacuum Rabi splitting  $g\sqrt{N}$  induced by the atoms, with  $g$  the single-photon Rabi frequency  $2g/(2\pi) = 21.8$  kHz. This means that the cavity-mediated dynamics of the atoms essentially conserves energy and can be well described by the following Hamiltonian:

$$\hat{H} = \hbar\chi\hat{j}_x^+\hat{j}_x^- + \hbar\Omega\hat{j}_x^+ - \hbar\delta\hat{j}_z \quad (1)$$

This Hamiltonian can be recast as the well known Lipkin–Meshkov–Glick (LMG) model<sup>25,26</sup>, which has been studied in various contexts, including quantum magnetism. In equation (1), we have introduced the collective spin operators  $\hat{j}_\alpha = \sum_j \hat{\sigma}_j^\alpha/2$ , where  $\hat{\sigma}_j^\alpha$  is a Pauli operator for the  $j$ th atom with  $\alpha = x, y, z$  and  $\hat{j}^\pm = \hat{j}_x \pm i\hat{j}_y$ . The summation runs over the individual atoms  $j = 1, \dots, N$  in the cavity. The parameter  $\chi$  sets the strength of the infinite-range exchange interactions mediated by the cavity mode, and  $\Omega$  and  $\delta$  define the strength of the transverse and longitudinal fields respectively (Fig. 1a). The model is realized in the limit in which the cavity field couples identically to all atoms trapped in the optical lattice (see Methods for modifications due to inhomogeneity in this coupling).

## Dynamical phase diagram of the LMG model

On varying the ratios between  $\Omega$ ,  $\delta$  and  $\chi$ , two distinct dynamical phases emerge, for which the time-averaged collective magnetization (along

$\hat{z}$ ) of the atomic ensemble  $\langle \hat{j}_z \rangle \equiv \lim_{T \rightarrow \infty} (1/T) \int_0^T \langle \hat{j}_z(t) \rangle dt$  serves as an order parameter. When all spins are initially prepared in the  $| \downarrow \rangle$  state and  $\delta = 0$ , the system features a sharp second-order transition<sup>43</sup> between a dynamical ferromagnetic phase with  $\langle \hat{j}_z \rangle \neq 0$  and a dynamical paramagnetic phase with  $\langle \hat{j}_z \rangle = 0$ . This transition is indicated by the solid green line ( $V_1$ ) on the phase diagram shown in Fig. 1b, as well as its projection on the  $\langle \hat{j}_z \rangle$  versus  $\Omega$  plane in the same panel and in Fig. 1c. More generally, as a function of the parameters  $\Omega$  and  $\delta/(\chi N) \geq -1/8$ , we observe a non-analyticity of the order parameter  $\langle \hat{j}_z \rangle$  (indicated by a solid white line in Fig. 1c), which marks a second-order transition between the two dynamical phases. However, the transition line is interrupted at a critical point  $\delta/(\chi N) = -1/8$ . Beyond this, there is a smooth crossover regime (indicated by a white dashed line in Fig. 1c) in which the system is ruled mainly by single-particle physics (set by  $\delta$  and  $\Omega$ ) and has an intermediate behaviour between that of a ferromagnet and a paramagnet.

In the ferromagnetic phase (red region in Fig. 1b and c), the instantaneous magnetization  $\langle \hat{j}_z \rangle$  oscillates about a non-zero time-averaged value, and the collective pseudospin Bloch vector  $\langle \hat{\mathbf{j}} \rangle \equiv (\langle \hat{j}_x \rangle, \langle \hat{j}_y \rangle, \langle \hat{j}_z \rangle)$  remains trapped below the equator of the Bloch sphere throughout the dynamics. This phase is dominated by the interactions which can be understood in a mean-field approximation as  $\chi\hat{j}^+\hat{j}^- \approx \chi(\hat{\mathbf{j}} \cdot \hat{\mathbf{j}} - \hat{j}_z^2) \approx \chi(N/2)(N/2 + 1) - 2\chi\langle \hat{j}_z \rangle \hat{j}_z$ . The term  $\hat{\mathbf{j}} \cdot \hat{\mathbf{j}}$  is a constant when restricted to the fully symmetric spin manifold, which is the case of interest here. The second term describes a self-induced precession of the collective Bloch vector about the  $\hat{z}$  axis, which effectively tilts the axis of rotation of the comparatively weak transverse field, such that the trajectory of the Bloch vector deforms into an orbit that remains below the equatorial plane.

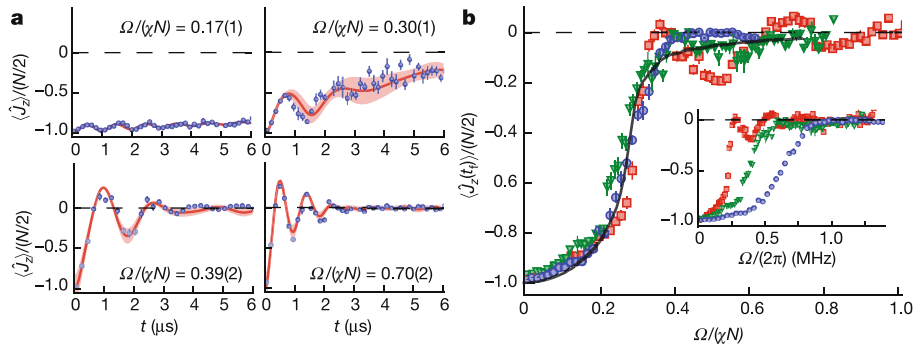


**Fig. 2 | Characteristic evolution of dynamical phases and scaling of DPT with atom number.** **a**, Time-traces of the mean magnetization  $\langle \hat{j}_z \rangle$  for the case of all spins initially on  $| \downarrow \rangle$ ,  $\delta = 0$  and  $\Omega$  quenched to different values, at  $t = 0$ , in the ferromagnetic (top panels) and paramagnetic (bottom panels) phases for  $N = 950 \times 10^3$  atoms and  $\Delta / (2\pi) = 50$  MHz. The experimental data (blue) are compared to theoretical calculations (red lines) based on a mean-field description including relevant experimental details (see Methods and Supplementary Information). Shaded theoretical region accounts for shot-to-shot fluctuations in  $\Omega / (\chi N)$ . Each point is the average of 12 experimental repetitions. **b**, Magnetization  $\langle \hat{j}_z(t_f) \rangle$  for different numbers of

atoms  $N = (935, 620, 320) \times 10^3$  (blue, green and red, respectively) after  $t_f = 4$   $\mu$ s of evolution for different normalized drive strengths  $\Omega / (\chi N)$  for  $\Delta / (2\pi) = 50$  MHz and  $\delta = 0$ . This measurement maps to the green solid line ( $V_1$ ) in Fig. 1b and c. The drive-strength normalization in each experimental shot is done by spin-dependent imaging. The solid black line indicates the simulated average (0–6  $\mu$ s) as a function of the normalized drive including dephasing sources. The inset shows the magnetization versus non-normalized transverse field strength  $\Omega$  for the same data sets. All error bars in experimental data are statistical ( $1\sigma$ ).

Conversely, the paramagnetic phase (blue region in Fig. 1b and c) is dominated by Rabi flopping driven by the transverse field  $\Omega \hat{j}_x$ . This term causes large oscillations of the instantaneous  $\langle \hat{j}_z \rangle$ , and, for  $\delta = 0$ , the collective Bloch vector breaks through the equatorial plane and rotates about the entire Bloch sphere.

For  $\delta = 0$ , the transition between the paramagnetic and ferromagnetic phases occurs at a critical drive  $\Omega_c = \chi N/2$ , as shown in Fig. 1b and c. The sharp transition in the dynamical behaviour of the system is traced back to the change in direction of the self-generated precession proportional to  $2\chi \langle \hat{j}_z \rangle \hat{j}_z$  as the Bloch vector crosses the equatorial plane at  $\langle \hat{j}_z \rangle = 0$ , generating an abrupt shift to large-amplitude oscillations for  $\Omega > \Omega_c$ . Typical dynamics of the collective Bloch vector in the ferromagnetic and paramagnetic phases are shown as insets in Fig. 1b. The solid green, solid blue and dashed blue lines in Fig. 1b and c indicate analogous trajectories in the phase diagram which will be explored experimentally later in Figs. 2b, 3a and 3b, respectively (see also Extended Data Fig. 2b and Supplementary Fig. 3 for investigation of the transition as a function of detuning and drive).

### Probing the LMG dynamical phase diagram

In our simulator, the cavity mediates a global spin-exchange interaction, which is microscopically described by a flip-flop process in which the emission of a photon from atom  $i$  in state  $| \uparrow \rangle$  into the cavity mode is subsequently absorbed by atom  $j$  in state  $| \downarrow \rangle$  (Fig. 1a, right). We operate in the regime  $|\Delta| \gg g\sqrt{N}$ , where the instantaneous average number of photons in the cavity mediating the interaction is much less than  $N$ , and the dynamics are well described by a spin-exchange model  $\chi \hat{j}^\dagger \hat{j}$  with coupling constant  $\chi = -g^2/\Delta$  (see also Extended Data Fig. 2a and Methods). Similarly, the large detuning means that superradiant emission does not play an active role, in contrast to previous work<sup>2</sup>. The interaction dynamics are faster than spontaneous emission,  $|\chi|N \gg \gamma$ , and satisfy the hierarchy  $|\Delta| \gg g\sqrt{N} \gg \kappa, \gamma$ .

We realize the transverse fields  $\Omega$  and  $\delta$  by injecting laser light at frequency  $\omega_p$  into the optical cavity through one mirror, creating a coherent driving field  $\Omega_p e^{i\omega_p t}$  inside the cavity. In the rotating frame at  $\omega_p$ , the laser light's detuning from atomic resonance  $\delta = \omega_p - \omega_a$  provides the longitudinal field  $\delta \hat{j}_z$  in equation (1). Moreover, the applied laser rapidly builds up a classical field within the cavity on a timescale of approximately  $1/\Delta$ , which couples  $| \downarrow \rangle$  to  $| \uparrow \rangle$ . This realizes the

transverse field  $\Omega \hat{j}_x$  in equation (1), where  $\Omega = -2g\Omega_p/\Delta$ . We adopt the convention that this transverse field is oriented along  $\hat{x}$  in the pseudospin coordinate system such that by jumping the phase of the laser light, we are able to create transverse fields oriented along any direction in the pseudospin  $x$ – $y$  plane. Furthermore, the experiment is realized with a standing wave cavity, where incommensurate lattice and drive wavelengths generate inhomogeneous  $\Omega$  and  $\chi$  parameters compared with the ideal case presented above. This leaves unchanged the generic features of the phase diagram in Fig. 1, but quantitatively modifies the phase boundary.

### DPT in absence of longitudinal field

In Fig. 2, we show experimental observations of the characteristic dynamics and DPT. We begin with all atoms in  $| \downarrow \rangle$  and then quench  $\Omega$  from zero to a specific value at  $t = 0$ . After a variable evolution time, we rapidly freeze the atomic dynamics by quenching  $\Omega \rightarrow 0$  and creating strong single-particle dephasing of the ground state. The atomic magnetization  $\langle \hat{j}_z \rangle$  and atom number  $N$  are then measured with high efficiency using fluorescence in combination with electron shelving and state-dependent displacements (see Methods and Extended Data Fig. 1).

For the time traces presented in Fig. 2a, we map the magnetization across different drive strengths with fixed  $\delta = 0$ . For drives deep in the ferromagnetic phase (Fig. 2a, top left), we observe small-amplitude oscillations that are in excellent agreement with our theoretical model based on a mean-field description of the system (see Methods and Supplementary Information). Close to the experimental critical point (Fig. 2a, top right and bottom left), the dynamics become more complicated owing to the complex interplay between interactions, drive and single-particle decoherence due to undesirable atomic motion in the optical lattice (see Supplementary Information and Supplementary Figs. 1 and 2). Deep in the paramagnetic phase (Fig. 2a, bottom right), we observe dynamics of the magnetization consistent with single-particle Rabi flopping with frequency  $\Omega$  and in good agreement with our simulation. Damping of the oscillations occurs predominantly because of inhomogeneity in the coupling of the spins to the common cavity mode, shot-to-shot fluctuations in  $\Omega / (\chi N)$  (attributed mostly to atom number fluctuations at about the 5% (root mean square, r.m.s.) level) and atomic motion in the lattice. Spontaneous emission and decoherence related to leakage of photons from the cavity are negligible. We include these

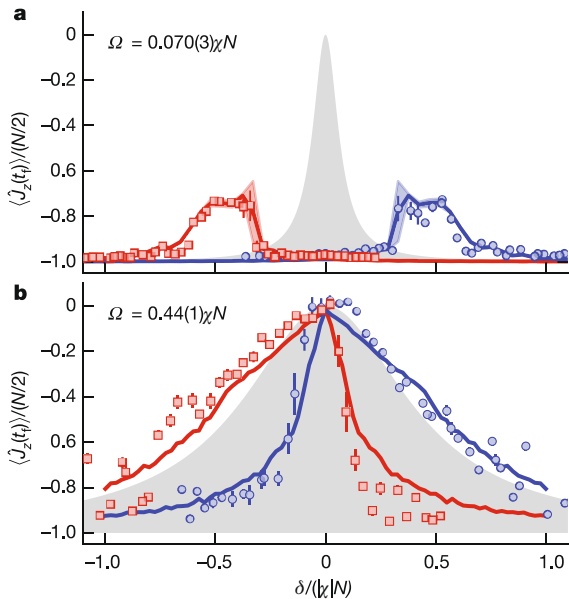


**Fig. 3 | Characterization of the DPT as a function of longitudinal field for two different transverse field values at fixed  $\chi N$ .** **a, b,** The atomic magnetization  $\langle j_z(t_f) \rangle$  at  $t_f = 4 \mu\text{s}$  is measured as a function of the normalized drive detuning  $\delta/(|\chi|N)$  for cavity detunings  $\Delta/(2\pi) = \pm 50 \text{ MHz}$  (red,  $+50 \text{ MHz}$ ; blue,  $-50 \text{ MHz}$ ) for two different drive strengths: **(a)**  $\Omega = 0.070(3)\chi N$  and **(b)**  $\Omega = 0.44(1)\chi N$ . The inner edges of the resonant features in **a** indicate a sharp transition from ferromagnetic to paramagnetic phases as  $|\delta|$  is increased. In contrast, the corresponding crossover in **b** is smoothed. Numerical simulations are shown as blue and red solid lines with corresponding shaded regions. The grey-shaded area indicates the non-interacting limit of Rabi flopping. Measurements in **a** and **b** map, respectively, to cuts represented by the blue lines  $H_1$  and  $H_2$  in Fig. 1b and c. All error bars in experimental data are statistical ( $1\sigma$ ).

effects in our theoretical model (Fig. 2a, red solid line), and fluctuations in  $\Omega/(\chi N)$  are indicated by the red shaded regions. Typically, we notice that the experimentally calibrated parameters overestimate the value of  $\Omega/(\chi N)$  by about 10% compared with the numerical simulations. We attribute this systematic disagreement to drifts on the calibration parameters and to details not captured by the theoretical model (see Supplementary Information).

We characterize the behaviour of the DPT with system size by measuring  $\langle j_z(t_f) \rangle$  at time  $t_f = 4 \mu\text{s}$  for different atom number  $N$  while initializing every atom in  $| \downarrow \rangle$  for  $\delta = 0$  in Fig. 2b. Measuring  $\langle j_z \rangle$  at a fixed time serves as a proxy of the long-term time-averaged magnetization, as considerable damping is caused by the previously mentioned effects. In the Fig. 2b inset, we observe a transition in the magnetization at different values of the transverse field  $\Omega$ , depending on atom number  $N$ . The dependence of the transition as a function of system size is demonstrated by re-scaling the corresponding drive as  $\Omega/(\chi N)$ , as shown in the main panel of Fig. 2b, analogous to the green curve in Fig. 1b and c. We observe collapse of the data and a critical drive  $\Omega_c^{\text{exp}} = 0.35(3)\chi N$ . A comparison to theoretical calculations using time-averaged magnetization (see Methods) shows reasonable agreement (solid black line). The shift of the critical point relative to the ideal collective model,  $\Omega/(\chi N) = 1/2$ , is predominantly attributable to the spatial inhomogeneity in the coupling of the atoms to the cavity mode (see Methods). Other small factors include single-particle decoherence of the atoms, which also contributes to the smearing out of the sharpness of the transition observed in the ideal system (Fig. 1b). Nevertheless, a clear transition can be observed, as shown by comparing to the theoretical calculation.

## DPTs at fixed transverse fields

The DPT can also be probed using our ability to controllably introduce a longitudinal field proportional to  $\delta j_z$  by detuning the injected light from the atomic transition, as shown in Fig. 1b. In Fig. 3, we map out the response of the system to the drive detuning  $\delta$  by measuring the order parameter  $\langle j_z(t_f) \rangle$  at  $t_f = 4 \mu\text{s}$  for two fixed values of the drive strength  $\Omega$  above and below the ( $\delta = 0$ ) critical point,  $\Omega_c^{\text{exp}}$ , and for two opposite cavity detunings  $\Delta/(2\pi) = \pm 50 \text{ MHz}$ .

We observe a sharp transition in the order parameter  $\langle j_z \rangle$  versus drive detuning, separating the ferromagnetic and the paramagnetic dynamical phases for a drive below the observed critical point  $\Omega_c^{\text{exp}}$  (blue solid line,  $H_1$ , in Fig. 1b and c). This is plotted in Fig. 3a with  $\Omega = 0.070(3)\chi N < \Omega_c^{\text{exp}}$ . We observe sharp transitions at the inside edges of the resonant features, which occur symmetrically for each  $\Delta$  at  $\delta_c/|\chi N| = \mp 0.27(2)$ . The critical value of  $\delta_c$  and the gradual decrease in  $\langle j_z \rangle$  for large detuning show good agreement with a mean-field calculation. The robustness of the sharp transition is demonstrated by the symmetric response of the magnetization for  $\Delta \leftrightarrow -\Delta$  and thus of the interaction shift  $\chi N \leftrightarrow -\chi N$ .

Conversely, when the drive is tuned above  $\Omega_c^{\text{exp}}$ ,  $\Omega = 0.44(1)\chi N > \Omega_c^{\text{exp}}$  (Fig. 3b), indicated by the blue dashed line,  $H_2$ , in Fig. 1b and c, we observe a smoother crossover between the paramagnetic and ferromagnetic phases about the detuning  $\delta_c/|\chi N| = \pm 0.04(3)$  in agreement with the mean-field calculation. Tuning  $\delta < \delta_c$  ( $\Delta > 0$ ) reduces the influence of the collective interactions, and the magnetization resembles the prediction of single-particle detuned Rabi flopping.

In both cases, the response of the system to  $\delta$  can be understood by interpreting the single-particle shift and interaction in equation (1) as a nonlinear detuning proportional to  $(2\chi \langle j_z \rangle + \delta) j_z$ , which competes with the coherent drive. Depending on the sign of the interaction and the instantaneous magnetization, the single-particle term  $\delta$  can either cancel or enhance the contribution of the interactions relative to the coherent drive, tuning the system between the ferromagnetic and paramagnetic dynamical phases. The predominant role of the interactions in the dynamics, especially below the critical point, can be observed by contrasting with the purely single-particle model of detuned Rabi oscillations (grey shaded area), which predicts a Lorentzian lineshape centred at  $\delta = 0$ .

## Sensitivity to initial condition

The single-particle control achievable in our experimental platform allows us to explore the DPT as a function of the initial state, as shown in Fig. 4. Specifically, we are able to demonstrate that the critical point of the transition is state-dependent, by preparing the collective pseudospin in different positions on the Bloch sphere. For example, we can prepare the system with  $\Omega < \Omega_c^{\text{exp}}$  such that the initial collective states near the south pole remained trapped below the equator, yet there also exist initial states prepared further towards the equator that exhibit large oscillations around the Bloch sphere characteristic of the paramagnetic phase.

Probing the response of the dynamics to different initial conditions allows us to establish a connection between the DPT in our effective spin model and the phenomena of macroscopic self-trapping and Josephson tunnelling observed in coupled atomic condensates<sup>28</sup> and solid-state polariton condensates<sup>29</sup>. Figure 4a schematically shows a double-well atomic condensate, where the initial magnetization of the collective state on the Bloch sphere is analogous to the initial population imbalance between the wells, while the azimuthal angle maps to the relative phase difference of the condensates. Similarly, the ferromagnetic and paramagnetic phases can be related to the self-trapped and tunnelling phases respectively<sup>41</sup>.

In Fig. 4c, we plot the measured magnetization after  $4 \mu\text{s}$  of evolution a polar projection of the Bloch sphere for different drive strengths  $\Omega$ ,

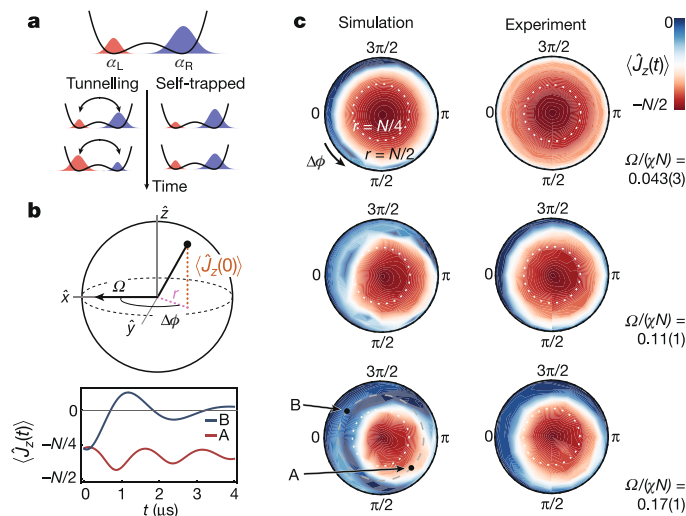


**Fig. 4 | Dependence of dynamical phases on initial conditions.** **a**, The initial state on the Bloch sphere and subsequent dynamics of the spin model can be mapped to that of atomic condensates in a double-well potential, described by coherent complex amplitudes in the left and right wells,  $\alpha_L$  and  $\alpha_R$ , respectively. Population imbalance maps to the magnetization ( $J_z \approx |\alpha_L|^2 - |\alpha_R|^2$ ) and the relative phase of the condensate wavefunctions maps to the azimuthal angle of the spin state ( $\Delta\phi$ ). As time evolves, the population imbalance either oscillates as atoms tunnel back and forth between the wells (tunnelling phase) or remains approximately constant (self-trapped phase). **b**, The initially prepared spin state can be parameterized in terms of the projection onto the equatorial plane  $r = \sqrt{(N/2)^2 - \langle J_z(0) \rangle^2}$  and the relative azimuthal phase  $\Delta\phi$  between the initial collective Bloch vector and the coherent drive (top; see Methods). The plot of  $\langle J_z(t) \rangle$  (bottom) indicates typical dynamics in the red and blue regions shown in the adjacent panel of **c**. **c**, Colour map of  $\langle J_z(t_f) \rangle$  at  $t_f = 4 \mu\text{s}$  of evolution, plotted in a polar projection of the Bloch sphere with coordinates defined by the initial condition as in **b** (initial conditions are always below the equator; they are shown above the equator in the figure to simplify visualization). Left (right) panels show simulated (experimental) results for  $\langle J_z(t_f) \rangle$  at  $t_f = 4 \mu\text{s}$  of evolution for different normalized drives  $\Omega/(\chi N)$ .

as we scan the initially prepared state  $\mathbf{J}(0)$ . Here, the radial coordinate maps to the magnitude of the projection of  $\mathbf{J}(0)$  on the equatorial plane (for  $\langle J_z(0) \rangle < 0$ ), and the angle  $\Delta\phi$  maps to the relative phase between the coherent drive and  $\mathbf{J}(0)$  (see Methods). As we increase the drive strength, the set of initial conditions that lead to the ferromagnetic phase shrinks (red region) while also becoming increasingly asymmetric about the south pole. Both of these features are in qualitative agreement with our theoretical calculations, also shown in Fig. 4c, which take into account coupling inhomogeneities, dephasing and shot-to-shot fluctuations on  $\Omega/(\chi N)$ . Quantitative differences are predominantly due to neglecting axial motion of the atoms in the theoretical model.

## Conclusion

The demonstration of the cooperation and competition between coherent drive and infinite-range interactions in an optical transition opens a path to the quantum simulation of richer spin models and out-of-equilibrium physics. For example, more complex spin–spin couplings can be engineered by using the available Zeeman sublevels of the  ${}^3\text{P}_1$  state with two different cavity polarizations<sup>3</sup>. Moreover, in the presence of additional inhomogeneous terms, our system can explore dynamical phases predicted to exist in Bardeen–Cooper–Schrieffer superconductors<sup>44,45</sup>, and by modulation of the transverse field our platform should be able to realize the archetypal model of a kicked top<sup>46</sup>, relevant for explorations of quantum chaos and scrambling dynamics<sup>47</sup>. Lastly, our investigation of non-equilibrium

dynamics with the  ${}^{88}\text{Sr}$  ( ${}^1\text{S}_0$ – ${}^3\text{P}_1$ ) optical transition can lead to insight into how to generate entangled states for quantum sensing with the long-lived  ${}^{87}\text{Sr}$  ( ${}^1\text{S}_0$ – ${}^3\text{P}_0$ ) optical transition used in state-of-the-art atomic clocks<sup>30</sup>.

## Online content

Any methods, additional references, Nature Research reporting summaries, source data, extended data, supplementary information, acknowledgements, peer review information; details of author contributions and competing interests; and statements of data and code availability are available at <https://doi.org/10.1038/s41586-020-2224-x>.

1. Leroux, I. D., Schleier-Smith, M. H. & Vuletić, V. Implementation of cavity squeezing of a collective atomic spin. *Phys. Rev. Lett.* **104**, 073602 (2010).
2. Norcia, M. A. et al. Cavity-mediated collective spin-exchange interactions in a strontium superradiant laser. *Science* **361**, 259–262 (2018).
3. Davis, E. J., Bentsen, G., Homeier, L., Li, T. & Schleier-Smith, M. H. Photon-mediated spin-exchange dynamics of spin-1 atoms. *Phys. Rev. Lett.* **122**, 010405 (2019).
4. Vaidya, V. D. et al. Tunable-range, photon-mediated atomic interactions in multimode cavity QED. *Phys. Rev. X* **8**, 011002 (2018).
5. Baumann, K., Guerlin, C., Brennecke, F. & Esslinger, T. Dicke quantum phase transition with a superfluid gas in an optical cavity. *Nature* **464**, 1301–1306 (2010).
6. Klinder, J., Keßler, H., Wolke, M., Mathey, L. & Hemmerich, A. Dynamical phase transition in the open Dicke model. *Proc. Natl. Acad. Sci. USA* **112**, 3290–3295 (2015).
7. Baden, M. P., Arnold, K. J., Grimsmo, A. L., Parkins, S. & Barrett, M. D. Realization of the Dicke model using cavity-assisted Raman transitions. *Phys. Rev. Lett.* **113**, 020408 (2014).
8. Ritsch, H., Domokos, P., Brennecke, F. & Esslinger, T. Cold atoms in cavity-generated dynamical optical potentials. *Rev. Mod. Phys.* **85**, 553–601 (2013).
9. Landini, M. et al. Formation of a spin texture in a quantum gas coupled to a cavity. *Phys. Rev. Lett.* **120**, 223602 (2018).
10. Kroeze, R. M., Guo, Y., Vaidya, V. D., Keeling, J. & Lev, B. L. Spinor self-ordering of a quantum gas in a cavity. *Phys. Rev. Lett.* **121**, 163601 (2018).
11. Kroeze, R. M., Guo, Y. & Lev, B. L. Dynamical spin–orbit coupling of a quantum gas. *Phys. Rev. Lett.* **123**, 160404 (2019).
12. Heyl, M., Polkovnikov, A. & Kehrein, S. Dynamical quantum phase transitions in the transverse-field Ising model. *Phys. Rev. Lett.* **110**, 135704 (2013).
13. Žunković, B., Heyl, M., Knap, M. & Silva, A. Dynamical quantum phase transitions in spin chains with long-range interactions: merging different concepts of nonequilibrium criticality. *Phys. Rev. Lett.* **120**, 130601 (2018).
14. Eckstein, M., Kollar, M. & Werner, P. Thermalization after an interaction quench in the Hubbard model. *Phys. Rev. Lett.* **103**, 056403 (2009).
15. Lamacraft, A. & Moore, J. in *Ultracold Bosonic and Fermionic Gases* (eds Levin, K. et al.) 177–202 (Elsevier, 2012).
16. Nandkishore, R. & Huse, D. A. Many-body localization and thermalization in quantum statistical mechanics. *Annu. Rev. Condens. Matter Phys.* **6**, 15–38 (2015).
17. Zhang, J. et al. Observation of a many-body dynamical phase transition with a 53-qubit quantum simulator. *Nature* **551**, 601–604 (2017).
18. Fláschner, N. et al. Observation of dynamical vortices after quenches in a system with topology. *Nat. Phys.* **14**, 265 (2018).
19. Jurcevic, P. et al. Direct observation of dynamical quantum phase transitions in an interacting many-body system. *Phys. Rev. Lett.* **119**, 080501 (2017).
20. Smale, S. et al. Observation of a transition between dynamical phases in a quantum degenerate Fermi gas. *Sci. Adv.* **5**, eaax1568 (2019).
21. Zhang, J. et al. Observation of a discrete time crystal. *Nature* **543**, 217–220 (2017).
22. Choi, S. et al. Observation of discrete time-crystalline order in a disordered dipolar many-body system. *Nature* **543**, 221–225 (2017).
23. Prüfer, M. et al. Observation of universal dynamics in a spinor Bose gas far from equilibrium. *Nature* **563**, 217–220 (2018).
24. Erne, S., Bücker, R., Gasenzer, T., Berges, J. & Schmidtmayer, J. Universal dynamics in an isolated one-dimensional Bose gas far from equilibrium. *Nature* **563**, 225–229 (2018).
25. Lipkin, H., Meshkov, N. & Glick, A. Validity of many-body approximation methods for a solvable model: (I). Exact solutions and perturbation theory. *Nucl. Phys.* **62**, 188–198 (1965).
26. Ribeiro, P., Vidal, J. & Mosseri, R. Thermodynamical limit of the Lipkin–Meshkov–Glick model. *Phys. Rev. Lett.* **99**, 050402 (2007).
27. Backhaus, S. et al. Discovery of a metastable-state in a superfluid  ${}^3\text{He}$  weak link. *Nature* **392**, 687–690 (1998).
28. Albiz, M. et al. Direct observation of tunneling and nonlinear self-trapping in a single bosonic Josephson junction. *Phys. Rev. Lett.* **95**, 010402 (2005).
29. Abbarchi, M. et al. Macroscopic quantum self-trapping and Josephson oscillations of exciton polaritons. *Nat. Phys.* **9**, 275–279 (2013).
30. Campbell, S. L. et al. A Fermi-degenerate three-dimensional optical lattice clock. *Science* **358**, 90–94 (2017).
31. Ludlow, A. D., Boyd, M. M., Ye, J., Peik, E. & Schmidt, P. O. Optical atomic clocks. *Rev. Mod. Phys.* **87**, 637–701 (2015).
32. Cazalilla, M. A. & Rey, A. M. Ultracold Fermi gases with emergent  $\text{SU}(n)$  symmetry. *Rep. Prog. Phys.* **77**, 124401 (2014).
33. Daley, A. J. Quantum computing and quantum simulation with group-II atoms. *Quantum Inform. Process.* **10**, 865 (2011).

34. Marino, J. & Diehl, S. Quantum dynamical field theory for nonequilibrium phase transitions in driven open systems. *Phys. Rev. B* **94**, 085150 (2016).

35. Barberena, D., Lewis-Swan, R. J., Thompson, J. K. & Rey, A. M. Driven-dissipative quantum dynamics in ultra-long-lived dipoles in an optical cavity. *Phys. Rev. A* **99**, 053411 (2019).

36. Mivehvar, F., Piazza, F. & Ritsch, H. Disorder-driven density and spin self-ordering of a Bose–Einstein condensate in a cavity. *Phys. Rev. Lett.* **119**, 063602 (2017).

37. Schiró, M. & Fabrizio, M. Time-dependent mean field theory for quench dynamics in correlated electron systems. *Phys. Rev. Lett.* **105**, 076401 (2010).

38. Sciolla, B. & Biroli, G. Quantum quenches and off-equilibrium dynamical transition in the infinite-dimensional Bose–Hubbard model. *Phys. Rev. Lett.* **105**, 220401 (2010).

39. Gambassi, A. & Calabrese, P. Quantum quenches as classical critical films. *Europhys. Lett.* **95**, 66007 (2011).

40. Smacchia, P., Knap, M., Demler, E. & Silva, A. Exploring dynamical phase transitions and prethermalization with quantum noise of excitations. *Phys. Rev. B* **91**, 205136 (2015).

41. Smerzi, A., Fantoni, S., Giovanazzi, S. & Shenoy, S. R. Quantum coherent atomic tunneling between two trapped Bose–Einstein condensates. *Phys. Rev. Lett.* **79**, 4950–4953 (1997).

42. Reinhard, A. et al. Self-trapping in an array of coupled 1D Bose gases. *Phys. Rev. Lett.* **110**, 033001 (2013).

43. Lerose, A., Žunkovič, B., Marino, J., Gambassi, A. & Silva, A. Impact of non-equilibrium fluctuations on pre-thermal dynamical phase transitions in long-range interacting spin chains. *Phys. Rev. B* **99**, 045128 (2019).

44. Barankov, R. A., Levitov, L. S. & Spivak, B. Z. Collective Rabi oscillations and solitons in a time-dependent BCS pairing problem. *Phys. Rev. Lett.* **93**, 160401 (2004).

45. Yuzbashyan, E. A., Dzero, M., Gurarie, V. & Foster, M. S. Quantum quench phase diagrams of an s-wave BCS–BEC condensate. *Phys. Rev. A* **91**, 033628 (2015).

46. Swingle, B., Bentsen, G., Schleier-Smith, M. & Hayden, P. Measuring the scrambling of quantum information. *Phys. Rev. A* **94**, 040302 (2016).

47. Swingle, B. Unscrambling the physics of out-of-time-order correlators. *Nat. Phys.* **14**, 988–990 (2018).

**Publisher's note** Springer Nature remains neutral with regard to jurisdictional claims in published maps and institutional affiliations.

© This is a U.S. government work and not under copyright protection in the U.S.; foreign copyright protection may apply 2020

## Methods

### Experimental description

Our experiment begins by loading up to  $10^6$   $^{88}\text{Sr}$  atoms from a magneto-optical trap into a one-dimensional optical lattice within an optical cavity, as we have described previously<sup>2,48–50</sup>. The lattice has wavelength 813 nm. This lattice is nominally near-magic with respect to the ultra-narrow millihertz  $^1\text{S}_0 \rightarrow ^3\text{P}_0$  clock transition at 698 nm, but can be made near-magic-wavelength for our optical transition at 689 nm ( $m_j=0$  states),  $^1\text{S}_0 \rightarrow ^3\text{P}_1$ , by setting the angle between the linear polarization of the lattice and the quantization axis. The near-magic wavelength reduces potential dephasing due to the transverse spreading of the atoms in a non-magic trap. We estimate residual inhomogeneous broadening due to the lattice to be below 2 kHz. The lattice spacing is incommensurate with the intracavity probe standing wave, leading to inhomogeneous coupling to the cavity mode. A sketch of the system is shown in Extended Data Fig. 1a. The atoms are laser-cooled to 14  $\mu\text{K}$  and trapped in the optical lattice, with typical axial trap oscillation frequency  $\omega_{\text{trap}}/(2\pi)=200$  kHz. The atom number is measured using fluorescence imaging on the dipole-allowed  $^1\text{S}_0 \rightarrow ^1\text{P}_1$  transition at 461 nm, and it is calibrated by comparing it with the vacuum Rabi splitting when the cavity is on resonance with the atomic transition ( $\Delta=0$ ), as detailed in ref.<sup>48</sup>. We determine  $\Delta=0$  and  $\delta=0$  from measurements of the symmetry of the collective vacuum Rabi splitting. The measured cavity linewidth is  $\kappa/(2\pi)=153.0(4)$  kHz. The cavity length is adjusted using piezoelectric actuators, such that it can be kept at a detuning  $\Delta$  during the experiment.

The cavity is driven for a time  $\tau$  by a near-resonant laser that realizes a coherent driving field  $\Omega_p e^{i\omega_p t}$  in the cavity, as shown in Extended Data Fig. 1, where  $\Omega_p$  is related to the input power  $P$  by the expression  $\Omega_p = \sqrt{\kappa_m P / (2\hbar\omega_p)}$ , with  $\kappa_m = \kappa T_m / (T_m + T_l)$ . Here, we define  $T_m$  and  $T_l$  as the single-mirror power transmission and loss coefficients, 105 ppm and 23 ppm respectively. The drive is turned on and off in approximately 10 ns using an in-fibre electro-optical modulator (EOM), which creates a sideband at detuning  $\delta$  while other frequency components are far from resonance and suppressed by being even further from resonance with the cavity mode. We apply a strong magnetic field perpendicular to the cavity axis to define the quantization axis. The probe light is polarized along the magnetic field direction such that the system is an effective two-level system  $|\downarrow\rangle = |^1\text{S}_0, m_j=0\rangle$  and  $|\uparrow\rangle = |^3\text{P}_1, m_j=0\rangle$  transition. For a more complete energy level diagram, see Extended Data Fig. 1c).

To observe the DPT, we need to be able to take a snapshot of the magnetization  $\langle j_z \rangle$  after some period of dynamical evolution. To achieve this, we have developed a technique to freeze the dynamics quickly and then apply state-dependent spatial displacements of the cloud such that the populations in the ground and excited states  $N_\downarrow$  and  $N_\uparrow$  are imaged on two different regions of a charge-coupled device (CCD) (Extended Data Fig. 1b).

After the drive is applied for some time  $\tau$ , as shown in the time sequence in Extended Data Fig. 1d, we turn off the coherent drive by extinguishing the applied EOM sideband. To effectively count atoms in both excited and ground state immediately after the drive, and freeze any dynamics that could be caused by spontaneous emission or the transient decay of the cavity field, we shine a strongly focused 461-nm beam along the  $\hat{z}$  axis and apply a strong 688-nm shelving beam. The 461-nm beam immediately stops the dynamics as it dephases the atoms, overwhelming the single particle rotation and any collective interactions. In addition, the 461-nm beam exerts a radiation pressure force that gives a momentum kick to the ground-state atoms, causing them to move away from the trapping region. Simultaneously, the shelving beam optically pumps excited-state atoms to the metastable  $^3\text{P}_{0,2}$  states (Extended Data Fig. 1c). We apply the shelving pulse for 5  $\mu\text{s}$ . For scale, at 2  $\mu\text{s}$ , we observe that >90% of the atoms in the excited state are shelved.

To finish our state-dependent detection, we allow for a short time of flight (about 100  $\mu\text{s}$ ) so that the momentum kick applied to the ground state atoms is translated into a displacement in space of a few 100  $\mu\text{m}$ . We then optically pump the shelved atoms back to  $^3\text{P}_1$  using 679-nm and 707-nm light applied for 200  $\mu\text{s}$ . The atoms then decay to the ground state via single-atom decay with time constant 21  $\mu\text{s}$ . We then perform fluorescence imaging for 50  $\mu\text{s}$  to observe the number of atoms in the two spatially resolved clouds as shown in Extended Data Fig. 1b. This allows us to measure the magnetization  $\langle j_z \rangle = (N_\downarrow - N_\uparrow) / (2(N_\downarrow + N_\uparrow))$  and total atom number  $N = N_\downarrow + N_\uparrow$  in a single shot. We found that the whole process efficiency is above 98%, limited mostly by the efficiency of the shelving process.

In Fig. 3, we change the drive detuning  $\delta$  by changing the frequency of the radiofrequency pulse applied to the EOM. The grey shaded area represents the r.m.s. amplitude for Rabi oscillations without interactions, that is,  $\chi=0$  in our model, and the corresponding r.m.s. magnetization is calculated simply as

$$\langle j_z \rangle_{\chi=0}^{\text{rms}} = -\frac{N}{2} \frac{\Omega^2}{(\delta^2 + \Omega^2)} - \frac{N}{2} \quad (2)$$

In Fig. 4, the initial state preparation is accomplished by preparing each spin in  $|\downarrow\rangle$  and then rotating the spins with a strong drive  $\Omega > \Omega_c$  for some chosen time. At this point,  $t=0$ , the system has acquired a magnetization  $\langle j_z(0) \rangle$ . We then simultaneously shift the phase of the driving field by  $\Delta\phi - \pi/2$  and its amplitude to some  $\Omega < \Omega_c$  and evolve for a fixed time, typically 4  $\mu\text{s}$ . The phase and amplitude jumps are accomplished by changing the phase and amplitude of the radiofrequency tone driving the EOM. We are then able to initialize the collective pseudospin Bloch vector at different positions on the Bloch sphere, such that  $\langle j_z(0) \rangle$  and  $\Delta\phi$  define the polar and the azimuthal angles, respectively, as indicated in the figure in the main text. As the phase of the driving field naturally defines the  $\hat{x}$  and  $\hat{y}$  axes for the spin degree of freedom, our protocol can equivalently be viewed as preparing the collective Bloch vector at analogous positions on the pseudospin Bloch sphere.

### Model and simulations

The dynamics of the experimental system are modelled by a master equation for the density operator  $\hat{\rho}$  of the complete atom–light system,

$$\frac{d\hat{\rho}}{dt} = -\frac{i}{\hbar} [\hat{H}_{\text{tot}}, \hat{\rho}] + \mathcal{L}_{\text{cl}}[\hat{\rho}] + \mathcal{L}_{\text{el}}[\hat{\rho}] + \mathcal{L}_{\text{s}}[\hat{\rho}] \quad (3)$$

Here, the Hamiltonian  $\hat{H}_{\text{tot}} = \hat{H}_A + \hat{H}_L + \hat{H}_{AL}$  is split into three contributions characterizing the atoms, pumping of the cavity field and atom–light interaction respectively:

$$\hat{H}_A = \frac{\omega_a}{2} \sum_i \hat{\sigma}_i^z \quad (4)$$

$$\hat{H}_L = \omega_c \hat{a}^\dagger \hat{a} + \Omega_p (\hat{a} e^{i\omega_p t} + \hat{a}^\dagger e^{-i\omega_p t}) \quad (5)$$

$$\hat{H}_{AL} = \sum_i g_i (\hat{a} \hat{\sigma}_i^+ + \hat{a}^\dagger \hat{\sigma}_i^-) \quad (6)$$

where  $\hat{a}$  ( $\hat{a}^\dagger$ ) is the annihilation (creation) operator of the cavity mode and the sums are taken over  $i = 1, \dots, N$  atoms. To reiterate,  $\omega_a$  is the frequency of the atomic transition,  $\omega_c$  the frequency of the relevant cavity mode,  $\Omega_p$  the effective amplitude of the injected field and  $\omega_p$  the corresponding frequency. The spatial dependence of the coupling is characterized by  $g_i = g \cos(k_i)$  and  $k = \pi \lambda_l / \lambda_c$ , where  $2g$  is the single-photon Rabi frequency at an antinode of the cavity mode. This form arises because the magic wavelength of the 1D optical lattice  $\lambda_l = 813$  nm is

incommensurate with the wavelength  $\lambda_c = 689$  nm of the cavity mode to which the atomic transition is coupled. For simplicity, we take the summation to run over  $i = 1, 2, \dots, N$  total lattice sites, such that each site is assumed to be occupied by only a single atom. In reality, there are about  $10^3$  relevant lattice sites, and each is occupied by about  $10^2$ – $10^3$  atoms, but as we assume contact interactions are not relevant and the atom–light coupling is consistent across the entire atomic sample, this simplification is reasonable.

Decoherence due to leakage of photons from the cavity at rate  $\kappa$  is described by the Lindblad term

$$\mathcal{L}_c[\hat{\rho}] = \frac{\kappa}{2} (2\hat{a}\hat{\rho}\hat{a}^\dagger - \hat{a}^\dagger\hat{a}\hat{\rho} - \hat{\rho}\hat{a}^\dagger\hat{a}) \quad (7)$$

while spontaneous emission on the atomic transition at rate  $\gamma$  and single-particle homogeneous broadening of the ensemble at rate  $\gamma_{\text{el}}$  are described by

$$\mathcal{L}_s[\hat{\rho}] = \frac{\gamma}{2} \sum_i 2\hat{\sigma}_i^-\hat{\rho}\hat{\sigma}_i^+ - \hat{\sigma}_i^+\hat{\sigma}_i^-\hat{\rho} - \hat{\rho}\hat{\sigma}_i^+\hat{\sigma}_i^- \quad (8)$$

$$\mathcal{L}_{\text{el}}[\hat{\rho}] = \frac{\gamma_{\text{el}}}{2} \sum_i \hat{\sigma}_i^z\hat{\rho}\hat{\sigma}_i^z - \hat{\rho} \quad (9)$$

The latter is attributed to a range of effects, including undesirable motion of the atoms in the optical lattice, and is discussed in more detail in the Supplementary Information.

The simulations presented in Figs. 2–4 are the result of numerical solution of equation (3) within the mean-field approximation (with the exception of the lower panels of Fig. 2a) which include additional effects due to axial motion that are discussed in the Supplementary Information. Specifically, we solve the equations of motion for  $\sigma_i \equiv \langle \hat{\sigma}_i^x \rangle, \langle \hat{\sigma}_i^y \rangle, \langle \hat{\sigma}_i^z \rangle$  and  $\langle \hat{a} \rangle$ , and factorize higher-order moments of the operators, for example,  $\langle \hat{\sigma}_i^x \hat{\sigma}_j^y \rangle \equiv \langle \hat{\sigma}_i^x \rangle \langle \hat{\sigma}_j^y \rangle$ . Further details regarding the numerical simulations can be found in the Supplementary Information.

The effective spin model that describes the nonlinear atomic dynamics throughout this manuscript is obtained from the atom–light model (equation (3)) by separate adiabatic elimination of the injected field and intracavity fluctuations, and the full calculation is detailed in the Supplementary Information. Here, we merely present the resulting Hamiltonian for the atoms:

$$\hat{H} = \hbar \sum_{i,j} \chi_{ij} \hat{\sigma}_i^+ \hat{\sigma}_j^- + \hbar \sum_i \frac{\Omega_i}{2} \hat{\sigma}_i^x - \frac{\hbar \delta}{2} \sum_i \sigma_i^z \quad (10)$$

where  $\chi_{ij} = -g_i g_j / \Delta$ ,  $\Omega_i = -2g_i \Omega_p / \Delta$  with  $\delta = \omega_p - \omega_a$  and  $\Delta = \omega_c - \omega_a$ . Moreover, we have assumed  $|\Delta| \gg \kappa, g, \sqrt{N}, \sqrt{g\Omega_p}, \delta$ . In the limit  $k = 2n\pi$  for  $n \in \mathbb{Z}$ , that is, uniform atom–light coupling  $g_j \rightarrow g$ , we recover the collective LMG model of equation (1).

Although in the experimental platform the atom–light coupling  $g_j$  is spatially varying owing to the incommensurate cavity and lattice wavelengths, the qualitative physics we explore is still consistent with the framework of the collective LMG model. Specifically, while the simulations of Figs. 2–4 take the proper form of  $g_j$  into account (see Supplementary Information), we observe that features of the detailed inhomogeneous model such as the critical point and dynamical timescales are consistent with the collective model upon a rescaling of the atom–light coupling.

For weak drives deep in the ferromagnetic phase, the collective model replicates the quantitative predictions of the inhomogeneous model upon replacement of the atom–light coupling with the r.m.s. average,  $g \rightarrow g/\sqrt{2}$  and thus  $\chi \rightarrow \chi/2$  and  $\Omega \rightarrow \Omega/2$ . This approximation is supported by comparison to experimental results for the period of the weak oscillations deep in the ferromagnetic phase, which are expected to be proportional to  $1/(\chi N)$ . In Extended Data Fig. 2a we extract this period

from the experimental data as a function of cavity detuning  $\Delta$ , which is equivalent to varying the interaction strength  $\chi \propto 1/\Delta$ . We confirm that the fitted slope agrees with the  $\chi \rightarrow \chi/2$  correction for inhomogeneous atom–light coupling.

As the drive is increased, the rescaling required for quantitative comparison changes. Specifically, comparing to the critical point  $\Omega_c^{\text{theory}}/(\chi N)$  obtained from a numerical calculation of the inhomogeneous model in the absence of decoherence, we find that the corresponding collective model requires a rescaling  $g \rightarrow 0.62g$ , and thus  $\chi \rightarrow 0.38\chi$  and  $\Omega \rightarrow 0.62\Omega$ , to match the critical value  $\Omega_c^{\text{theory}}/(\chi N) \approx 0.31$ . The reduction of this value below the true collective critical drive  $\Omega_c/(\chi N) = 1/2$  is consistent with that observed experimentally ( $\Omega_c^{\text{exp}}/(\chi N) = 0.35(3)$ ).

## Mapping the phase boundary

In Fig. 1b, c, we present the system phase diagram (under the assumption of uniform atom–light coupling), where we map the magnetization  $\langle \hat{j}_z \rangle$  as a function of the probe detuning  $\delta$  and drive amplitude  $\Omega$ . A sharp boundary separates the dynamical phases for  $\Omega/(\chi N) \lesssim 0.65$ , shown by the solid white line in Fig. 1c. However, as the drive is further increased and for  $\delta/(\chi N) < -1/8$ , the boundary becomes a smooth crossover, as shown by the dashed white line in Fig. 1c.

Using similar results to those shown in Fig. 3, for the inhomogeneous case relevant for experiment we are able to map out this boundary and define a critical detuning  $\delta_c$  between the two dynamical phases for different fixed drive strengths  $\Omega$ . We identify these values by looking at the maximum gradient on each of the experimental and numerical  $\langle \hat{j}_z \rangle$  against  $\delta$  plots shown in Fig. 3. In Extended Data Fig. 2b we plot  $\delta_c$  against  $\Omega$  (points) and compare with numerical simulations (solid lines) for two opposite cavity detunings  $\Delta/(2\pi) = \pm 50$  MHz. For values above  $\Omega/(\chi N) \approx 0.31$ , the solid traces do not represent a strict phase boundary but rather characterize the crossover region, analogous to the crossover region in Fig. 1c for the homogeneous case.

In the Supplementary Information, we derive an expression for the boundary between the two dynamical phases based on the model presented in equation (1) in the mean field limit. In the homogeneous case, the phase boundary  $\Omega_c(\delta)$  is, for  $\delta/(\chi N) > -1/8$ :

$$\frac{\Omega_c(\delta)}{\chi N} = \frac{1}{2} \left[ 2 \left( 1 - \frac{\delta}{\chi N} \right) \left( 1 + \frac{2\delta}{\chi N} \right) - \frac{3}{2} \left( \frac{8\delta}{\chi N} + 1 \right) + \frac{1}{2} \left( 1 + \frac{8\delta}{\chi N} \right)^{3/2} \right]^{1/2} \quad (11)$$

To address the inhomogeneous coupling present in our experiment, we rescale  $g \rightarrow 0.62g$  and thus  $\chi \rightarrow 0.38\chi$  and  $\Omega \rightarrow 0.62\Omega$  in this equation as described earlier. A comparison of the rescaled equation (11) to the experimental data is shown as the black traces in Extended Data Fig. 2b for two different detunings.

## Data availability

Data relevant to the figures and conclusions of this manuscript are available at <https://doi.org/10.5061/dryad.mgqnk98w9><sup>51</sup>.

## Code availability

The codes used in the analysis of experimental data and to carry out associated theoretical calculations are available from the corresponding authors upon reasonable request.

48. Norcia, M. A. & Thompson, J. K. Strong coupling on a forbidden transition in strontium and nondestructive atom counting. *Phys. Rev. A* **93**, 023804 (2016).
49. Norcia, M. A. et al. Frequency measurements of superradiance from the strontium clock transition. *Phys. Rev. X* **8**, 021036 (2018).
50. Norcia, M. A., Winchester, M. N., Cline, J. R. K. & Thompson, J. K. Superradiance on the millihertz linewidth strontium clock transition. *Sci. Adv.* **2**, e1601231 (2016).
51. Muniz Silva, J. A. et al. Exploring dynamical phase transitions with a cavity-QED platform, v2. Dryad dataset (2020); <https://doi.org/10.5061/dryad.mgqnk98w9>.

# Article

**Acknowledgements** We acknowledge discussions with I. Spielman, M. Holland and A. Shankar. This work is supported by the Air Force Office of Scientific Research (AFOSR) grant FA9550-18-1-0319, by the Defense Advanced Research Projects Agency (DARPA) Extreme Sensing and ARO grant W911NF-16-1-0576, the ARO single investigator award W911NF-19-1-0210, the US National Science Foundation (NSF) PHY1820885, NSF JILA-PFC PHY-1734006 grants, and by the National Institute of Standards and Technology (NIST). J.R.K.C. acknowledges financial support from NSF GRFP.

**Author contributions** J.A.M., D.J.Y., J.R.K.C. and J.K.T. collected and analysed the experimental data. R.J.L.-S., D.B. and A.M.R. developed the theoretical model. All authors discussed the results and contributed to the preparation of the manuscript.

**Competing interests** The authors declare no competing interests.

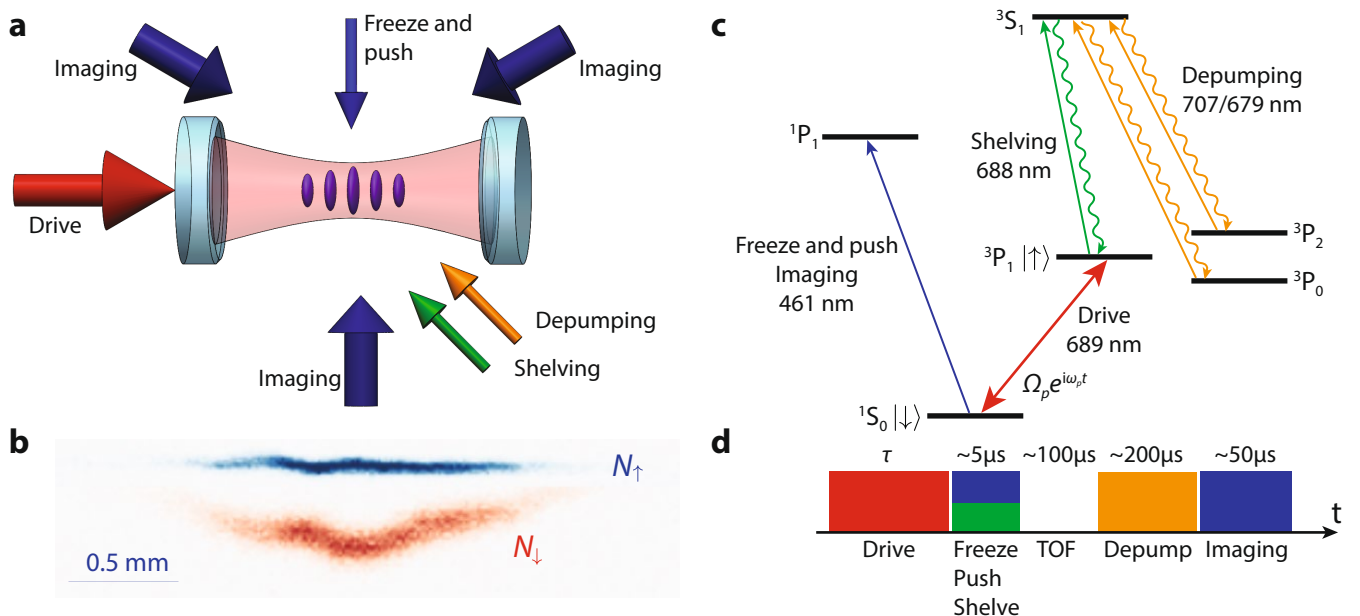
**Additional information**

**Supplementary information** is available for this paper at <https://doi.org/10.1038/s41586-020-2224-x>.

**Correspondence and requests for materials** should be addressed to A.M.R. or J.K.T.

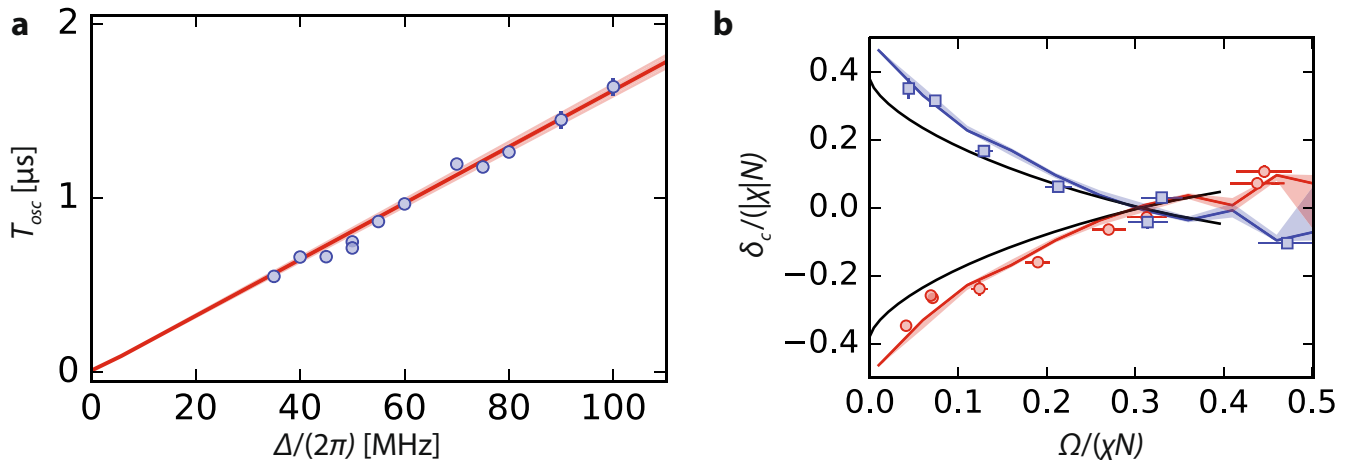
**Peer review information** *Nature* thanks Murray Barrett, Maria Luisa Chiofalo and Farokh Mivehvar for their contribution to the peer review of this work.

**Reprints and permissions information** is available at <http://www.nature.com/reprints>.



**Extended Data Fig. 1 | Experimental platform.** **a**, An optical cavity is driven by a 689-nm coherent field that establishes an intra-cavity field  $\Omega_p e^{i\omega_p t}$ , which is near resonance with the  $^1S_0$  to  $^3P_1$  transition in  $^{88}\text{Sr}$ . Inside the cavity, an ensemble of atoms is confined in a 1D optical lattice at 813 nm. Different lasers are applied for shelving excited-state atoms into long-lived metastable excited states, for freezing the system dynamics, for applying a radiation pressure force that pushes ground states in a direction transverse to the cavity axis, for optically pumping atoms from long lived metastable excited states back to the ground state, and for fluorescence imaging of atoms in the ground state.

**b**, A typical fluorescence image captured on a CCD, showing the state-resolved imaging technique. The  $N_e$  excited state atoms that were shelved into  $^3P_{0,2}$  while the freeze/push beam was applied remain near the trapping region. The  $N_g$  ground-state atoms are pushed away from the trapping region. Based on their spatial location, the atoms assigned to be in the excited (ground) state are shown in false colour blue (orange). **c**, The relevant energy levels for  $^{88}\text{Sr}$ , the laser wavelengths and their functions. **d**, Experimental timing sequence and typical timescales.



**Extended Data Fig. 2 | Probing many-body dynamics and mapping the phase boundary.** **a**, Oscillation period as function of the cavity detuning  $\Delta$  for  $2\Omega_p/(Ng) = 0.104(4)$ ,  $\delta = 0$  and atoms starting in  $|↓\rangle$ . Blue points are experimental values, solid red line represents the mean-field prediction for the same drive and atom number, and the shaded red area represents typical experimental fluctuations on  $2\Omega_p/(Ng)$ . The period is extracted from sinusoidal fits to data as in Fig. 2a, after removing a linear term caused by the single-particle dephasing effects. The mean-field value (red solid line) is

$T_{\text{osc}} = 2\pi/(N\gamma)$  with the effective replacements due to inhomogeneous coupling as discussed in Methods. Measurements are taken in the dispersive limit where  $\Delta \gg \sqrt{Ng}$ . **b**, Critical detuning  $\delta_c$  as function of the drive  $\Delta$  for  $\Delta/(2\pi) = \pm 50$  MHz (red and blue points, respectively). We also plot the theoretical prediction for the phase boundary (equation (11)) with rescaled parameters, and predictions of the numerical model (solid lines) including uncertainty based on the typical fluctuations in  $\Omega/(\chi N)$ . Error bars are statistical ( $1\sigma$ ).